Title

Effective mechanical potential of cell–cell interaction explains three-dimensional morphologies during early embryogenesis

Short title

Cell–cell mechanical potential for morphogenesis

Authors

Hiroshi Koyama[1,2,*], Hisashi Okumura[2,3,4], Atsushi M. Ito[2,5], Kazuyuki Nakamura[7,8], Tetsuhisa Otani[2,6], Kagayaki Kato[2,9,10], and Toshihiko Fujimori[1,2]

[1]Division of Embryology, National Institute for Basic Biology, 5-1 Higashiyama, Myodaiji, Okazaki, Aichi 444-8787, Japan

[2]SOKENDAI (The Graduate University for Advanced Studies), Hayama, Kanagawa 240-0193, Japan

[3]Biomolecular Dynamics Simulation Group, Exploratory Research Center on Life and Living Systems (ExCELLS), National Institutes of Natural Sciences, 5-1 Higashiyama, Myodaiji, Okazaki, Aichi 444-8787, Japan

[4]Institute for Molecular Science, National Institutes of Natural Sciences, 5-1 Higashiyama, Myodaiji, Okazaki, Aichi 444-8787, Japan

[5]National Institute for Fusion Science, National Institutes of Natural Sciences, 322-6 Oroshi-cho, Toki, Gifu 509-5292, Japan

[6]Division of Cell Structure, National Institute for Physiological Sciences, 5-1 Higashiyama, Myodaiji, Okazaki, Aichi 444-8787, Japan

[7]School of Interdisciplinary Mathematical Sciences, Meiji University, 4-21-1 Nakano, Nakano-ku, Tokyo 164-8525, Japan

[8]JST, PRESTO, 4-1-8 Honcho, Kawaguchi, Saitama 332-0012, Japan

[9]Bioimage Informatics Group, Exploratory Research Center on Life and Living Systems (ExCELLS), National Institutes of Natural Sciences, 38 Nishigonaka, Myodaiji, Okazaki, Aichi 444-8585, Japan

[10]Laboratory of Biological Diversity, National Institute for Basic Biology, 38 Nishigonaka, Myodaiji, Okazaki, Aichi 444-8585, Japan

*Correspondence: Hiroshi Koyama

Division of Embryology, National Institute for Basic Biology, 5-1 Higashiyama, Myodaiji, Okazaki, Aichi 444-8787, Japan

Phone: +81 564 59 5862,

hkoyama@nibb.ac.jp.

Author contribution

H.K. designed the work, H.K., A.M.I., and H.O. contributed to the conception. H.K. and T.F. designed experiments, and H.K. performed experiments and image processing. H.K. and H.O. designed models, H.K. developed computational algorithms, and H.K. and K.N. statistically analyzed the data. H.K., T.O., H.O., A.M.I., K.N., K.K., and T.F. wrote the manuscript, and all authors contributed to the interpretation of the results.

Conflicts of interest

The authors declare no competing financial interests.

Keywords

effective potential of cell–cell interaction, morphological diversity, mechanics, emergent property of multicellular system, mouse pre-implantation embryo

This file includes:

Main text

Figure 1 to 8

Abstract

Mechanical forces are critical for the emergence of diverse three-dimensional morphologies of multicellular systems. However, it remains unclear what kind of mechanical parameters at cellular level substantially contribute to tissue morphologies. This is largely due to technical limitations of live measurements of cellular forces. Here we developed a framework for inferring and modeling mechanical forces of cell–cell interactions. First, by analogy to coarse-grained models in molecular and colloidal sciences, we approximated cells as particles, where mean forces (i.e. effective forces) of pairwise cell–cell interactions are considered. Then, the forces were statistically inferred by fitting the mathematical model to cell tracking data. This method was validated by using synthetic cell tracking data resembling various *in vivo* situations. Application of our method to the cells in the early embryos of mice and the nematode *Caenorhabditis elegans* revealed that cell–cell interaction forces can be written as a pairwise potential energy in a manner dependent on cell–cell distances. Importantly, the profiles of the pairwise potentials were quantitatively different among species and embryonic stages, and the quantitative differences correctly described the differences of their morphological features such as spherical vs. distorted cell aggregates, and tightly vs. non-tightly assembled aggregates. We conclude that the effective pairwise potential of cell–cell

interactions is a live measurable parameter whose quantitative differences can be a parameter describing three-dimensional tissue morphologies.

Author summary

Emergence of diverse three-dimensional morphologies of multicellular organisms is one of the most intriguing phenomena in nature. Due to the complex situations in living systems (e.g. a lot of genes are involved in morphogenesis.), a model for describing the emergent properties of multicellular systems has not been established. To approach this issue, approximation of the complex situations to limited numbers of parameters is required. Here, we searched for mechanical parameters for describing morphologies. We developed a statistical method for inferring mechanical potential energy of cell–cell interactions in three-dimensional tissues; the mechanical potential is an approximation of various mechanical components such as cell–cell adhesive forces, cell surface tensions, etc. Then, we showed that the quantitative differences in the potential is sufficient to reproduce basic three-dimensional morphologies observed during the mouse and *C. elegans* early embryogenesis, revealing a direct link between cellular level mechanical parameters and three-dimensional morphologies. Our framework provides a noninvasive tool for measuring spatiotemporal cellular forces, which would be useful for studying

103 morphogenesis of larger tissues including organs and their regenerative therapy.

104

105

Introduction

In multicellular living systems, various three-dimensional morphologies are observed in tissues and organs, which are often tightly linked to their physiological functions. Morphogenetic events are thought to be primarily dependent on the mechanical properties of the constituent cells [1–5]. Mechanical parameters such as cell–cell adhesion energy and cell surface tensions are involved in morphogenetic events including compartmentalization of different cell populations, epithelial cell movements etc. However, mechanical parameters which give rise to a variety of three-dimensional morphologies remain to be elucidated. If such parameters are identified, we can understand not only mechanical principles of emergent properties of multicellular systems during morphogenesis but also easily simulate three-dimensional tissues in a predictable manner, which may be valuable for regenerative therapy.

To search for mechanical parameters which are directly linked to three-dimensional morphologies, we focused on mechanical potential energies of pairwise cell–cell interactions as follows. Cell–cell adhesion forces, which are mediated by cell adhesion molecules such as cadherin proteins, can be approximated as attractive forces in isolated two cell systems (Fig. 1A-i and -ii), whereas both excluded volume effect of cells and actomyosin-mediated cell surface tensions can be as repulsive forces [1,2,4,6–8]; due

124 to cell volume conservation, two cells cannot extremely approach each other, and the cell
125 surface tensions can antagonize cell–cell adhesion forces. Because the summation of
126 these forces would be dependent on cell–cell distance (Fig. 1A-iii), it is written by
127 pairwise potential energy (Fig. 1A-iv, distance–potential curve). There may be factors
128 other than the above affecting the pairwise potentials. In molecular and colloidal sciences,
129 pairwise potentials of objects such as amino acids are considered, and the profiles of the
130 distance–potential curves are critical for the behaviors of systems [9,10]. In multicellular
131 systems, the pairwise potentials are conceptually well-known [7,8,11,12]. But the profiles
132 have been never measured nor inferred in multicellular systems, and therefore,
133 researchers arbitrarily set the profiles in theoretical studies (e.g. hard- or soft-core
134 potentials, etc.) [13–16]. Theoretical studies related to morphogenesis did not assume
135 substantial differences in the profiles [17–20]. However, considering the case of
136 molecular/colloidal sciences, we speculated that the profiles substantially determine the
137 systems' behaviors or morphologies in certain multicellular systems.

138 To examine whether the profiles of pairwise potentials can determine
139 morphologies of multicellular systems, quantitative measurements/inferences of the
140 profiles in real tissues are inevitable. In the case of isolated two cell systems, adhesive
141 forces between two cells were experimentally measured (i.e. forces required to dissociate

one cell from the other) [4,21], but their pairwise potentials were not determined. Importantly, due to complex situations in real tissues compared with isolated two cell systems, it is unknown whether pairwise potentials are correctly defined and detectable *in vivo*. On the other hand, in molecular and colloidal sciences, we found a strategy worth considering: a top-down approach is adopted for inferring pairwise potentials, where positions of the objects such as radial distribution functions are solely used [10,22].

In the present study, we develop a top-down method for inferring pairwise potentials of cell-cell interactions by using movements of cells obtained from three-dimensional time lapse imaging (Fig. 1B). Briefly, a theoretical model considering force values of cell–cell interactions were fitted to the cell tracking data. Our method was validated by using various synthetic data which were generated by simulations under pregiven cell–cell interaction forces. Then, we applied our method to the blastomeres in the *C. elegans* and mouse early embryos, and successfully detected pairwise potentials of cell–cell interactions. We discovered quantitative differences in the profiles of the inferred potentials among the embryos, and showed that, through simulations, the differences were linked to the embryos' morphological features. Note that applicability of our method to other cell types such as epithelial cells and self-migratory cells is beyond the scope of the present study. We assume that the nearly-spherical cell shape of blastomeres may be well-

approximated by particle models, while the highly deformed cell shapes of epithelial or mesenchymal cells may not be suitable. This issue will be discussed later in the Discussion section with the limitations of our method.

Theory and principle for inferring effective potential

Particle-based cell models

To infer effective forces of cell–cell interactions *in vivo*, we developed a particle-based model in which the particles interact with each other and attractive or repulsive forces (F_i) are assumed as shown in Fig. 1B-i; i is an identifier for particle–particle interactions. In three-dimensional cellular systems with no attachment to substrates, we did not assume persistent random walks which originate from cellular traction forces on substrates [23,24].

The equation of particle motions is defined below. In cellular-level phenomena, viscous drag force or frictional force provided by the surrounding medium or tissue is dominant, as expected from the low Reynolds number; consequently, the inertial force is negligible in general [3,7,25–27]. The forces in such a system can be assumed to be correlated with the velocities of the objects [3,14,25,28,29]. Thus, the velocity ($V_{C|p}$) of a particle is calculated by the net force ($F_{C|p}$) exerted on the particle as follows (Fig. 1B-i):

$$V_{C|p} = F_{C|p} / \gamma \qquad \text{(Eq. 1)},$$

where p is an identifier for particles and γ is the coefficient of viscous drag and frictional forces. $F_{C|p}$ is the summation of cell–cell interaction forces exerted on the pth particle. We

184 assumed the simplest situation, i.e., γ is constant (=1.0). Thus, by giving the values of F_i
185 from, for instance, a distance–potential curve, a simulation can run. In addition, γ may not
186 be constant in real tissues, while it is challenging to measure the value with spatial
187 resolution at cellular level [30].
188
189 *Data acquisition of time series of cell positions*
190 To define cell positions, we focused on nuclei, because they are most easily
191 imaged by microscopy (Fig. 1B-ii) in a wide range of organisms from *C. elegans* to
192 mammals, and these data are accumulating [31–35]. We utilized publicly available
193 nuclear tracking data of a developing embryo of *C. elegans* [31]; nuclear tracking data of
194 developing mouse embryos were obtained in this study.
195
196 *Development of method for inferring effective potentials/forces of cell-cell interaction*
197 In the case of ions, molecules, etc., radial distribution functions are often used to
198 infer the effective potentials of their interactions [10,22]. This method is simple, but is
199 only applicable to thermodynamically equilibrium systems because this function reflects
200 the effective potentials under equilibrium states. Therefore, this method is not suitable for
201 non-equilibrium systems, including morphogenetic events. To infer the effective

potentials in non-equilibrium systems, we fitted the particle-based cell model to the time series of nuclear positions, where the fitting parameters are forces between all pairs of cell–cell interactions for each time frame (Fig. 1B-iii). We systematically searched for the values of the effective forces between all pairs of cell–cell interactions that minimized the differences (i.e. corresponding to least squares) between the particle positions in the simulations and the *in vivo* nuclear positions. The differences (G_{xyz}) to be minimized are defined as follows.

$$G_{xyz} = \sum_{t=1}^{T} \sum_{p=1}^{P(t)} \frac{\left\{x_p(t) - x_p^{\mathrm{ref}}(t)\right\}^2 + \left\{y_p(t) - y_p^{\mathrm{ref}}(t)\right\}^2 + \left\{z_p(t) - z_p^{\mathrm{ref}}(t)\right\}^2}{\Delta t}$$

(Eq. 2)

Here, p is an identifier for particles, t is an identifier for time frames, and Δt is the time interval between the time frames. T is the total time frame, and $P(t)$ is the number of particles at each time frame. The x, y, and z coordinates of the pth particle obtained from microscopic images are x_p^{ref}, y_p^{ref}, and z_p^{ref}; ref means reference. The coordinates of the simulations are x_p, y_p, and z_p. Note that, because γ was assumed to be constant in Equation 1, we can only infer relative but not absolute values of effective forces.

To determine whether our method can correctly infer effective forces, we applied it to synthetic data generated by simulations under given potentials of particle–particle interactions, and examined whether the inferred effective forces were consistent with the

given potentials. Unfortunately, Equation 2 did not work well: the inferred forces were not consistent with given potentials. In particular, even around the longer cell–cell distance, the force values did not decay (Fig. S2). Therefore, we tried to incorporate various additional constraints into Equation 2. We found that the following cost function worked well: the function was set so that force values approach zero at long distant regions of cell–cell interactions as defined below:

$$G = G_{xyz} + G_{F_0} \qquad (G_{F_0} = \omega_{F_0} \sum_{t=1}^{T} \sum_{i=1}^{I(t)} \psi(D_i) F_i^2 \Delta t) \qquad \text{(Eq. 3)},$$

where F_i is the force value of ith cell–cell interactions, $I(t)$ is the total number of the cell–cell interactions for each time frame, D_i is the cell–cell distance of the ith interaction, and ω_{F_0} is a coefficient for determining the relative contribution of the second term to G. $\Psi(D_i)$ is a distance-dependent weight that exponentially increases and eventually becomes extremely large, leading to that the value of F_i approaches zero especially around larger D_i (Fig. S1A-iii). We show validations of this cost function in the next sections. Detailed procedures are described in Supplementary Information (Section 4).

Results

Systematic validation of inference method using simulation data

We systematically validated our inference method using simulation data. We

238 used the Lenard–Jones (LJ) potential as a test case of the given potentials (Fig. 2A-i), and
239 generated simulation data under LJ potential, to which we applied our inference method.
240 Importantly, we assumed cell-intrinsic mechanical activities that were introduced as
241 fluctuations of the forces relative to the LJ potential (Fig. 2A-i, "fluctuation (% of LJ)"),
242 because the cells rapidly stop movements without such activities.

243 In Fig. 2A-i, the particles were initially scattered to some extent, and then
244 assembled. The inferred effective forces for each pair of particles for each time frame
245 were plotted against particle–particle distances (Fig. 2A-ii, heat map), and by calculating
246 binned averages, we obtained distance–force (DF) curves (Fig 2A-ii, yellow). In the
247 absence of the fluctuations, the data points were located around the DF curve (Fig. 2A-ii,
248 standard deviation (SD) = 0%), and the DF curve showed a similar profile to that from
249 the LJ potential (Fig. 2A-iii, LJ vs. 0%). In the presence of the fluctuations (SD = 100 or
250 1,000%), although the data points were widely distributed (Fig. 2A-ii), the resultant DF
251 curves were equivalent to that of the LJ potential and of that under SD = 0% (Fig. 2A-iii).
252 We also quantitatively evaluated the differences of the force values between the inferred
253 DF and the LJ potential by calculating L2 norm which is described in the legend; i.e., L2
254 norm = $\{F_{\mathrm{inferred}}(D) - F_{\mathrm{LJ}}(D)\}^2$, where F_{inferred} and F_{LJ} are the force values from the
255 inferred DF and the LJ potential, respectively. These results suggest that our method is

256 correctly applicable for assembling process even under large fluctuations of the forces.
257 Effect of ω_{F_0} in Equation 3 is shown in Fig. S2. In addition to the LJ potential, we also
258 tested other potentials (e.g., Morse potential) and the inferred DF curves were similar to
259 the given potentials (Fig. S2 and S3).

260 In Fig. 2B, effective DF curves were inferred in systems under steady states
261 where particles continuously moved due to the force fluctuations (SD = 1,000%). The
262 inferred DF curves showed an almost similar profile to that of the LJ potential (Fig. 2B-
263 ii, sampling interval = 1min), but increased sampling intervals caused inconsistency with
264 the LJ potential (sampling interval = 5 min).

265 In Fig. 2C, effective DF curves were inferred in systems with cell proliferation
266 where cell numbers were increased from 38 to 47; handling of cell proliferation/division
267 is described in the Supplementary information with the case of dead/lost cells. The
268 inferred DF curves showed a similar profile to that of the LJ potential (Fig. 2C-ii), and
269 the influence of the sampling interval was similar to Fig. 2B.

270 These results suggest that our method can correctly infer the forces of cell–cell
271 interactions in three-dimensional cell aggregates. Note that long sampling intervals cause
272 incorrectness of the inference in practice. In addition, around longer cell–cell distances,
273 the inferred DF curves showed slight inconsistencies with the LJ potential in the case of

274 Fig. 2B and 2C but not 2A. This may be caused by crowding, because the particles in Fig.
275 2A were sparsely distributed compared with Fig. 2B and 2C.
276
277
278 *Spatial constraints had no influence on effective forces*
279 Next, we assessed the applicability of our method to systems with spatial
280 constraints resembling the zona pellucida or eggshells, which the mouse and *C. elegans*
281 embryos possess. The particles with the LJ potential were put into spherocylindrical
282 constraints (Fig. 3-i). In longer lengths of spherocylinders, inferred DF curves were well
283 consistent with the DF curves from the LJ potential (Fig. 3-ii; length of spherocylinder ≥
284 25μm). These results indicate that DF curves are correctly inferred under spatial
285 constraints.
286 By contrast, under shorter spherocylinders, the profiles of inferred DF curves
287 were shifted leftward along the distance (Fig. 3-ii; length of spherocylinder ≤ 20μm). In
288 these cases, the particles were compressed, and their movements were significantly
289 restricted as follows. The mean diameter of the particles roughly corresponds to the
290 distance providing the potential minimum (Fig. 1A-iii and -iv). In Fig. 3-i, the particle
291 diameters were depicted to be equivalent to the mean diameter of cells, and, under the

292 condition of the length = 16μm, the distances between the adjacent particles seemed to be
293 less than the diameter of the particles. Moreover, the positions of the particles were not
294 changed but fixed throughout the simulations (Fig. 3-i, 16μm), and showed a well-aligned
295 array resembling a closed-packed state (Fig. 3-i, broken lines). Compressive states are
296 observed in real tissues such as spheroids [29,36,37], whereas we do not know the
297 existence of tissues where cell movements are absolutely restricted by spatial constraints;
298 if such tissues existed, DF curves could be affected by the constraints.
299
300
301 *Effective pairwise potentials were detected in C. elegans early embryo*
302 We next investigated whether effective potential could be detected as a function
303 of cell–cell distance in three-dimensional *in vivo* systems. The nematode *C. elegans*
304 exhibits well-defined embryogenesis: cell movements in early embryos are almost
305 identical among different individuals, and the time series of nuclear positions have been
306 reported previously [31]. During early *C. elegans* embryogenesis, a fertilized egg (i.e. one
307 cell) repeatedly undergoes cell division and cell differentiation in a stiff/undeformable
308 eggshell, ultimately forming an ovoid embryo containing ~350 cells (Fig. 4A-B, and
309 Movie S1A). The cells become smaller through cell division [38], and the total volume

310 of the embryo remains constant. Thus, the volume of each cell is reduced by a factor of
311 350 relative to the original egg, meaning that mean cell diameter is reduced by a factor of
312 7 (Fig. 4B; e.g., the diameter at *t* (time frame) = 195 is ~28% of that at *t* = 16). Because
313 the mean diameter of particles is approximately reflected on a DF curve (Fig. 1A-iii and
314 -iv), we expected that inferred DF curves should be gradually shifted to the left side of
315 the distance–force graph throughout embryogenesis.

316 Figure 4C are snapshots at different time points, that show nuclear positions with
317 inferred effective forces where the color of the lines corresponds to the values of the
318 forces (Movie S1B). Note that, in our inference in this system, we confirmed that this
319 inference problem has essentially a unique solution (Fig. 4D); the uniqueness of solutions
320 is important to judge whether the inferred result is plausible in fitting problems as
321 previously discussed [39,40]. We divided the whole embryogenesis into segments
322 containing different time frames, and examined whether DF curves were detectable. Fig.
323 4E is an example of the DF curve (binned average) at *t* = 76-115 with all data points
324 shown as a heat map. Although the data points were widely distributed similar to the
325 previous figures (Fig. 2A-ii), a clear DF curve was detected as shown by yellow. The DF
326 curve exhibited a typical profile with regions of repulsive and attractive forces (Fig. 4F, *t*
327 = 76-115). Similarly, we successfully detected the DF and DP (distance–potential) curves

328 for each period (Fig. 4F, t = 16–55, 36–75, 76–115, 116–155, and 156–195). These curves
329 were gradually shifted toward the left side, as we had theoretically expected, indicating
330 that the inferred effective potentials were quantitatively consistent with the reduction in
331 cell volume during embryogenesis. To evaluate differences in mechanical properties
332 among the periods, we normalized both the distances and potentials by the distances at
333 the potential minima (Fig. 4G); the potentials were divided by the square of the distances
334 at the potential minima. The curves were almost unchanged during the periods, suggesting
335 that the mechanical properties of cell–cell interactions are not drastically modulated
336 during the development except for the cell sizes. Although slight deviations were
337 observed for the stages t36-75 and t76-115, whether this represents changes in the
338 mechanical properties in the embryo requires further investigation.

339 We also compared the profiles of the inferred DP curves with previously used
340 ones. The framework of the Morse potential is often considered (e.g. Fig. S3) [13,18,20],
341 while other frameworks were presented [14,16,20,29,41]. We fitted these frameworks to
342 our inferred DP curves. The Morse potential often fitted with small discrepancies,
343 whereas the potential presented by Delile et al. [20] usually showed larger discrepancies
344 (Fig. S7). This is because the Morse potential is quite flexible (i.e., various profiles are
345 generated according to their parameter values), while the Delile's potential sets a narrower

range of cell–cell distances where attractive forces can be exerted.

Model dependency of inference in C. elegans embryo

Next, we evaluated a model-dependency. In our particle model, the viscous frictional forces were assumed to be proportional to the absolute velocities of the particles as previously presented (Eq. 1). On the other hand, some papers argued that the viscous frictional forces should be determined by the velocities relative to surrounding particles [29,36]. The equation of motions in this model is as follows; $F_{\mathrm{C}|p} = \sum_{m=1}^{N}[\{\omega_{\mathrm{g}}(D_{pm})\gamma\}\{(V_{\mathrm{C}|p} - V_{\mathrm{C}|m})\bullet e_{pm}\}e_{pm}]$, where m is the ID of particles interacting with the pth particle and $V_{\mathrm{C}|m}$ is the velocity of the mth particle; see the Supplementary information in detail. The difference between the two models comes from whether the viscous frictional forces originate from non-moving objects (e.g., liquid medium, substrate) or moving objects (e.g., neighboring cells). Fig. S8 shows the comparison of the inferred DP curves between the two models, which were almost similar profiles each other. We guess that, in systems where cell populations exhibit collective migration (i.e., similar velocities among the cells), the model choice may become significant, and, during the developmental stages in the early *C. elegans* embryo, collective migration may rarely

occur.

Effective pairwise potentials were detected in mouse pre-implantation embryos

To further investigate whether effective forces were detectable in three-dimensional real systems, we focused on mouse pre-implantation embryos, including the 8-cell and compacted morula stages (Fig. 5A, illustration). In 8-cell stage embryos before compaction, cell–cell adhesion is weak, and individual cells can be easily discerned (Fig. 5A, bright field). In the compaction-stage embryos composed of ~16-32 cells, cell–cell adhesion becomes stronger due to elevated expression of cadherin proteins on cell membrane, and the cells are strongly assembled [42]. The surface of the embryo becomes smooth, and the embryonic shape becomes more spherical (Fig. 5A, bright field). We performed cell tracking (Fig. 5A, tracking) and inferred effective forces. We successfully detected effective DF and DP curves for the two stages (Fig. 5B and S9 for other embryos), which showed typical profiles with regions of repulsive and attractive forces. Compaction-stage embryos include inner and outer cells differentiating to different cell types [43]. We calculated DF curves for three pairs of interactions (inner–inner, outer–outer, and inner–outer), and found that the profiles of the curves were different each other

382 (Fig. S10).

383

384 *Effective potentials were capable of describing morphologies*

385 To examine whether effective pairwise potentials can be a parameter for
386 determining morphologies, we performed simulations based on the inferred potentials
387 from the *C. elegans* and mouse embryos. In simulations of multicellular systems, the
388 simulation outcomes are determined by both DF curves and initial configurations,
389 because energetic local minimum states (i.e. metastable state) as well as global minimum
390 states are meaningful. To find stable states under the DF curves, we performed
391 simulations starting from various initial configurations of the particles (Fig. 6A, two
392 different initial configurations are shown), and the systems were relaxed.

393 From the DF curves of the *C. elegans* embryos, we observed a tendency that the
394 particles form an aggregate with an ovoid or distorted shape (Fig. 6A). These results may
395 be consistent with experimental observations: the embryonic cells can keep a cell
396 aggregate even when the eggshell is removed, and subsequent culture leads to a cell
397 aggregate with an ovoid or distorted shape, except for very early stage of development (<
398 ~20 cells) [44,45]. From the DF curves of the mouse 8-cell stage embryos, an aggregate
399 was generated (Fig. 6B). From the DF curves of the mouse embryos at the compaction

400 stage, a spherical aggregate was generated (Fig. 6B); this morphology is consistent with
401 the *in vivo* situation. Therefore, the effective potentials from the *C. elegans* and mouse
402 embryos yielded different morphologies. These results suggest that all of the DF curves
403 are capable of recapitulating the basic morphological features of the systems.
404
405 *Robustness of simulation outcomes*
406 As shown above, the ovoid/distorted shape or spherical shape were generated in a manner
407 dependent on DF curves. We examined whether our inference robustly results into the
408 same simulation outcomes. During the minimization of the cost function G, we sampled
409 DF curves before reaching the minimum of G. Fig. 6B shows the DF curves for the *C.*
410 *elegans* embryo t36-75 (left panel), and their values of G are plotted against the maximum
411 attractive force in the DF curves (right panel); the colors in the two panels correspond
412 each other. Before reaching the minimum (a red line in left panel and a red circle in the
413 right), the DF curves exhibited some differences in their profiles (red vs. light blue or
414 purple). Then, simulations were performed from an initial configuration which shows a
415 cuboid shape (bottom panel, "start"). For all the DF curves tested, the particles were not
416 spherically assembled but the initial cuboid shape was almost sustained. By contrast, in
417 the case of the mouse compaction stage shown in Fig. 6C, the particles were spherically

418 assembled for all the DF curves except for an intermediate sample (light blue) which
419 shows two isolated aggregates. These results suggest that simulation outcomes resulting
420 from our inference are robust, and the DF curves are sufficient to explain morphologies
421 among different tissues.
422
423 *Effective pairwise potentials were different between compacted and non-compacted*
424 *mouse embryo*
425 To evaluate the predictive capability of the DF curves inferred by our method,
426 we performed perturbation experiments. In the mouse compaction stage, the cells are
427 tightly assembled to form a spherical and symmetric embryonic shape. In other words,
428 we think that there are two morphological features, 1) increase in symmetry of the
429 embryos, and 2) smoothing of the embryonic surfaces. The embryos are surrounded by
430 external structures called zona pellucida which have negligible effects on morphogenesis
431 [46 and reference therein]. Because both E-cadherin and actomyosin are essential for the
432 compaction process [42,47,48], we inhibited these proteins by chemicals: EDTA
433 (ethylenediaminetetraacetic acid) for E-cadherin, cytochalasin D for F-actin, and
434 blebbistatin for non-muscle myosin II (Fig. 7A).
435 The effective DP curves were inferred under these drugs (Fig. 7B and S12 with

436 enlarged views). Then, we quantitatively evaluated the differences among the DP curves,
437 and found that the distances at the potential minima were increased under the three
438 inhibitors (Fig. 7C, left panel). Because the distances at the potential minima are related
439 to the mean diameters of cells (Fig. 1A-iv), this result predicted that the distances between
440 adjacent cells were increased. This prediction was supported through histological
441 observations: each cell exhibited a nearly spherical shape and seemed that the cells were
442 not so densely assembled especially under the condition of EDTA compared with the no-
443 drugs condition (Fig. 7D). The embryonic and cellular shapes are schematically depicted
444 in Figure 7E. In addition, we found another quantitative difference among the DP curves,
445 related to decay of attractive forces. We measured distances at 10% energy of potential
446 minima as relative values to the distances at the potential minima, and found that the
447 relative distances were decreased under EDTA and blebbistatin (Fig. 7C, right panel, and
448 S14A). This result means that attractive forces of long-range interactions were reduced
449 under these drugs.
450
451 *Effective pairwise potential described compacted and non-compacted morphologies in*
452 *mouse embryo*
453 Simulations under the DP curves from the drugs-treated embryos were

454 performed. The cell particles were spherically or almost spherically assembled under the
455 potentials of the normal embryos or the cytochalasin D-treated embryos, respectively (Fig.
456 8A). By contrast, the cell particles were not spherically assembled under the potentials of
457 the EDTA or blebbistatin-treated embryos. All simulation data are provided in Figure
458 S15A from which representative results are shown in Fig. 8A.

459 To uncover what kinds of the profiles of the DP curves are linked to
460 morphological changes in the compaction process, we first introduced two indices for the
461 morphologies as follows. Sphericity ($=(36\pi V^2)^{1/3}/S$) is essentially defined as the ratio of
462 volume (V) to surface area (S) so that the value becomes 1.0 for spheres. Shapes other
463 than spheres show values less than 1.0. Thus, both the increases in symmetry and in
464 smoothness of surfaces contribute to this index. Aspect ratio is defined as the ratio of the
465 length of the longest axis to that of the shortest axis in an ellipsoid which is fitted to an
466 object of interest. The increase in symmetry leads to that the aspect ratio becomes 1.0,
467 and otherwise the aspect ratio shows more than 1.0. The sphericities of all simulation
468 outcomes in Figure 8A and S15A were measured, and we found that the sphericities were
469 decreased under EDTA and blebbistatin (Fig. 8B, left panel). Similarly, the aspect ratios
470 were increased under EDTA and blebbistatin (Fig. 8C, left panel).

471 We searched for parameters which can describe the sphericities or aspect ratios.

Among several parameters tested, the distances at potential minima measured in Figure 7C showed a tight relationship to the sphericities (Fig. 8B, right panel). The sphericities showed an abrupt change along the x-axis. These results indicate that the sphericity is the order parameter for the morphological transition of the compaction process and that the distance at the potential minimum is the control parameter. On the other hand, the relative distances at 10% potential minima showed a clear relationship to the aspect ratios (Fig. 8C, right panel). Thus, the morphological transitions of the compaction process are induced by the quantitative changes in the DP curves.

Discussion

In this study, we developed a top-down method for statistically inferring effective potentials of cell–cell interactions using cell tracking data. We then demonstrated that effective potentials are detectable as a function of cell–cell distances in real tissues. Our findings provide for the first time the experimental quantification of effective potentials, which have been recognized conceptually [7,8]. Furthermore, effective potentials with quantitative differences in their profiles can be a critical parameter for morphologies; ovoid vs. spherical, compacted vs. non-compacted.

490 Moreover, the experiments using inhibitors suggest that effective potentials can be a
491 measure for evaluating mechanical properties of cells including mutants in a noninvasive
492 manner.
493
494 *Morphology of embryo*
495 For the generation of spherical/circular tissues, tissue surface tension is involved
496 in [1,29,49,50]. The surface tension reduces surface area of tissues in analogy to liquid
497 droplets. Therefore, when non-spherical cell aggregates are provided, they show a
498 tendency to round up to spherical shapes, where tissue surface tension contributes to the
499 dynamics (i.e., the speed of the rounding-up) [49,51]. Although the presence of tissue
500 surface tension may be a typical property of tissues [1,29], tissues do not always exhibit
501 spherical shapes including the *C. elegans* embryos whose eggshells are removed [44,45].
502 Similarly, the drugs-treated mouse embryos showed a morphological transition from a
503 spherical shape to a non-spherical shape after adding the drugs (Fig. S11). These data
504 mean that tissue surface tension is not a sole determinant, but there are other factors
505 significantly contributing to tissue shapes which can overcome the effect of the tensions.
506 Note that cell–cell adhesion forces contribute to both tissue surface tension [26,50] and
507 the pairwise potential of cell–cell interactions (Fig.1), suggesting that the pairwise

508 potential relates to tissue surface tension.

509 In addition, the EDTA-treated mouse embryos harbor intercellular spaces (Fig.
510 7D and S13), in which we do not think that tissue surface tensions are correctly defined.
511 Our result identified a parameter which explains sphericity of such tissues (Fig. 8B).
512 Similar tissues with intercellular spaces are also known in other species and tissues
513 including zebrafishes [52].

514

515 *Comparison of other inference methods with other models*

516 To understand morphogenetic events, mechanical states and simulations based
517 on those states are essential. Models such as vertex, Cellular Potts, and phase field models
518 are often utilized, especially for epithelial cells [3,53–56]. These models successfully
519 recapitulated various morphogenetic events, including cell sorting, epithelial cell
520 movements/rearrangements, the formation of the mouse preimplantation embryos [53,57],
521 and very early embryogenesis in *C.elegans* [58]. However, it is still challenging to
522 measure cellular and non-cellular parameters in three-dimensional systems with high
523 spatiotemporal resolution, although high-resolution inferences of parameters such as cell–
524 cell junction tensions and stresses have been performed in two-dimensional situations by
525 fitting a vertex model to experimental observations [40,59]. In addition, because the

526 assumptions of the vertex model are based on epithelial cells, its application to other cells
527 is limited including blastomeres and mesenchymal cells. On the other hand, particle
528 models are mainly used for cell aggregates and mesenchymal/self-propelled cells [12,14],
529 while some papers applied particle models to epithelial cells [15,18,19,60], meaning that
530 the applicability of particle models is expanding. Due to its simplicity of particle models
531 (i.e. low degrees of freedom), our method can provide a framework for quantitatively
532 connecting model parameters to *in vivo* parameters under three-dimensional situations.
533 Possibilities of image-based inference methods are expanding under three-dimensional
534 situations [61].
535
536 *Limitation and perspective of our inference method*
537 In the present study, we applied our inference method to blastomeres.
538 Applicability of our method to other cell types including epithelial and mesenchymal cells
539 will be evaluated. Epithelial cells are usually modeled by the vertex models where each
540 cell is assumed to be polygonal, and many-body (i.e. ≥3 cells) interactions but not
541 pairwise ones are considered [62,63]. By using the vertex model, the highly deformable
542 features of epithelial cells are well reproduced. It remains unknown whether pairwise
543 potentials can be a good approximation of epithelial cells, though three-dimensional

544 epithelial cells were modeled by particle-based models, which enabled one to simulate
545 three-dimensionally large tissues [15,18,19,64]. In deformable objects such as cells, cell–
546 cell interaction forces show hysteresis; i.e., the forces at the same distance become
547 different between the cases when two cells are approaching and dissociating. This effect
548 may be expressed by different profiles of DF curves between the two cases. In the vertex
549 models, this hysteresis is implemented through its high deformability. Because our
550 inference method contains temporal information of cell–cell interaction forces, it may be
551 possible to examine whether systems show hysteresis. It would be worth investigating
552 whether the framework of two DF curves based on the hysteresis can expand the
553 capability of particle models for describing various phenomena.

554 In our inference method, the coefficient of viscous frictional forces is considered
555 as described in Equation 1. Typically, this coefficient is assumed to be constant in
556 multicellular models. However, the values of this coefficient and its spatiotemporal
557 distributions in real tissues remain poorly understood [30]. There can be many factors
558 affecting the coefficient; e.g., cell–cell contact area, cell size, the number of contacting
559 cells per one cell, cell–cell adhesion molecules including cadherins, surface structures of
560 cells [65–67]. In the second model presented in the *C. elegans* embryos (Fig. S8), the
561 number of contacting cells per one cell is effectively considered. Influence of cell–cell

adhesion molecules means that the coefficient is different among cell types (e.g., differentiated vs. undifferentiated cells, etc.). Unfortunately, experimental measurements of the coefficient with spatiotemporal resolution are lacking.

A serious issue to be considered is possible influence of external factors on inference results. We showed that spatial constraints such as eggshells were negligible. On the other hand, there are many external factors in real tissues such as expanding liquid cavities in cystic structures such as the mouse blastocysts, traction forces exerted between cells and extracellular matrices (ECM) which leads to self-migratory activities, cell–ECM adhesions which leads to cell spreading, and so on [53,68,69]. It is important to evaluate whether these factors affect inferred results or not, and this issue holds true about other inference methods based on model fitting approaches (e.g. the vertex model-fitting described above). Unfortunately, it is often technically challenging to directly measure the spatiotemporal effect of the external factors on cell movements, otherwise, we can correctly infer cell–cell interaction forces by subtracting the effect of the external factors. Although overcoming this situation with many degrees of freedom is challenging, we speculate that the analogy to molecular and colloidal sciences can be helpful. In these fields, systems including external factors (e.g. solvents, pressures, etc.) can be successfully approximated as effective pairwise potentials of particle–particle

interactions to some extent which are informative for predicting the systems' behaviors. We are planning to examine what kinds of external factors can be approximated as effective pairwise potentials, leading to establishment of a framework for simulating larger tissues/organs in a minimal model.

Materials and methods

Details of experimental procedures, mathematical modeling, and statistical methods are described in Supplementary Information.

Acknowledgement

We thank Drs. Jean-François Joanny, Hiroaki Takagi and Yasuhiro Inoue for critical reading of the manuscript. We thank Dr. Yoshitaka Kimori for helpful discussions. We thank Ms. Azusa Kato for supporting nuclear tracking. This work was supported by following grants: Japan Ministry of Education, Culture, Sports, Science and Technology Grant-in-Aid for Scientific Research on Innovative Areas "Cross-talk between moving cells and microenvironment as a basis of emerging order" for H.K., the National Institutes of Natural Sciences (NINS) program for cross-disciplinary science study for H.K., and a Japan Society for the Promotion of Science (JSPS) Grant-in-Aid for Young Scientists (B)

for H.K. (17K15131).

References

1. Steinberg MS. Differential adhesion in morphogenesis : a modern view. Curr Opin Genet Dev. 2007;17: 1281–286. doi:10.1016/j.gde.2007.05.002
2. Guillot C, Lecuit T. Mechanics of epithelial tissue homeostasis and morphogenesis. Science (80-). 2013;340: 1185–9. doi:10.1126/science.1235249
3. Fletcher AG, Osterfield M, Baker RE, Shvartsman SY. Vertex models of epithelial morphogenesis. Biophys J. 2014;106: 2291–2304. doi:10.1016/j.bpj.2013.11.4498
4. Maître J-L, Berthoumieux H, Krens SFG, Salbreux G, Jülicher F, Paluch E, et al. Adhesion Functions in Cell Sorting by Mechanically Coupling the Cortices of Adhering Cells. Science (80-). 2012;338: 253–256. doi:10.1126/science.1225399
5. Bazellières E, Conte V, Elosegui-artola A, Serra-picamal X, Bintanel-morcillo M, Roca-cusachs P, et al. Control of cell–cell forces and collective cell dynamics by the intercellular adhesome. Nat Cell Biol. 2015;17: 409–420.

doi:10.1038/ncb3135

6. Yong J, Moeller J, Hart KC, Ramallo D, Vogel V, Dunn AR, et al. Spatial distribution of cell–cell and cell–ECM adhesions regulates force balance while maintaining E-cadherin molecular tension in cell pairs. Mol Biol Cell. 2015;26: 2456–2465. doi:10.1091/mbc.E14-12-1618

7. Forgacs G, Newman SA. Biological Physics of the Developing Embryo. Cambridge University Press; 2005.

8. Merkel M, Manning ML. Using cell deformation and motion to predict forces and collective behavior in morphogenesis. Semin Cell Dev Biol. 2017;67: 161–169. doi:10.1016/j.semcdb.2016.07.029

9. Atkins P, Paula J De, Keeler J. Atkins' Physical Chemistry. 11th ed. Oxford University Press; 2018.

10. Israelachvili JN. Intermolecular and Surface Forces. 3rd ed. Elsevier Inc.; 2011.

11. Weikl TR, Asfaw M, Krobath H, Bartosz R, Lipowsky R. Adhesion of membranes via receptor–ligand complexes: Domain formation, binding cooperativity, and active processes. Soft Matter. 2009;5: 3213–3224. doi:10.1039/b902017a

12. Ranft J, Basan M, Elgeti J, Joanny J-F, Prost J, Jülicher F. Fluidization of tissues

by cell division and apoptosis. Proc Natl Acad Sci U S A. 2010;107: 20863–20868. doi:10.1073/pnas.1011086107

13. D'Orsogna MR, Chuang YL, Bertozzi AL, Chayes LS. Self-Propelled Particles with Soft-Core Interactions : Patterns , Stability , and Collapse. Phys Rev Lett. 2006;96: 104302. doi:10.1103/PhysRevLett.96.104302

14. Szabó B, Szöllösi GJ, Gönci B, Jurányi Z, Selmeczi D, Vicsek T. Phase transition in the collective migration of tissue cells: Experiment and model. Phys Rev E. 2006;74: 061908. doi:10.1103/PhysRevE.74.061908

15. Sepúlveda N, Petitjean L, Cochet O, Grasland-Mongrain E, Silberzan P, Hakim V. Collective Cell Motion in an Epithelial Sheet Can Be Quantitatively Described by a Stochastic Interacting Particle Model. PLoS Comput Biol. 2013;9: e1002944. doi:10.1371/journal.pcbi.1002944

16. Belmonte JM, Thomas GL, Brunnet LG, de Almeida RMC, Chate H. Self-Propelled Particle Model for Cell-Sorting Phenomena. Phys Rev Lett. 2008;100: 248702. doi:10.1103/PhysRevLett.100.248702

17. Drasdo D, Kree R, McCaskill JS. Monte Carlo approach to tissue-cell populations. Phys Rev E. 1995;52: 6635–6657.

18. Nissen SB, Rønhild S, Trusina A, Sneppen K. Theoretical tool bridging cell

polarities with development of robust morphologies. Elife. 2018;7: e38407. doi:10.7554/elife.38407

19. Nissen SB, Perera M, Gonzalez JM, Morgani SM, Jensen MH, Sneppen K, et al. Four simple rules that are sufficient to generate the mammalian blastocyst. PLoS Biol. 2017;15: e2000737. doi:10.1371/journal.pbio.2000737

20. Delile J, Herrmann M, Peyriéras N, Doursat R. A cell-based computational model of early embryogenesis coupling mechanical behaviour and gene regulation. Nat Commun. 2017;8: 13929. doi:10.1038/ncomms13929

21. Kashef J, Franz CM. Quantitative methods for analyzing cell–cell adhesion in development. Dev Biol. 2015;401: 165–174. doi:10.1016/j.ydbio.2014.11.002

22. Pettitt BM, Rossky PJ. Alkali halides in water: Ion–solvent correlations and ion–ion potentials of mean force at infinite dilution. J Chem Phys. 1986;84: 5836–5844. doi:10.1063/1.449894

23. Garcia S, Hannezo E, Elgeti J, Joanny JF, Silberzan P, Gov NS. Physics of active jamming during collective cellular motion in a monolayer. Proc Natl Acad Sci U S A. 2015;112: 15314–15319. doi:10.1073/pnas.1510973112

24. Basan M, Elgeti J, Hannezo E, Rappel W-J, Levine H. Alignment of cellular motility forces with tissue flow as a mechanism for efficient wound healing. Proc

Natl Acad Sci. 2013;110: 2452–2459. doi:10.1073/pnas.1219937110

25. Li X, Balagam R, He T-F, Lee PP, Igoshin OA, Levine H. On the mechanism of long-range orientational order of fibroblasts. Proc Natl Acad Sci. 2017;114: 8974–8979. doi:10.1073/pnas.1707210114

26. Schötz E, Burdine RD, Jülicher F, Steinberg MS, Heisenberg CP, Foty RA. Quantitative differences in tissue surface tension influence zebrafish germ layer positioning. HFSP J. 2008;2: 42–56. doi:10.2976/1.2834817

27. He B, Doubrovinski K, Polyakov O, Wieschaus E. Apical constriction drives tissue-scale hydrodynamic flow to mediate cell elongation. Nature. 2014;508: 392–396. doi:10.1038/nature13070

28. Arboleda-Estudillo Y, Krieg M, Stühmer J, Licata NA, Muller DJ, Heisenberg CP. Movement Directionality in Collective Migration of Germ Layer Progenitors. Curr Biol. 2010;20: 161–169. doi:10.1016/j.cub.2009.11.036

29. Basan M, Prost J, Joanny J-F, Elgeti J. Dissipative particle dynamics simulations for biological tissues: rheology and competition. Phys Biol. 2011;8: 026014.

30. Zhu M, Tao H, Samani M, Luo M, Wang X, Hopyan S, et al. Spatial mapping of tissue properties in vivo reveals a 3D stiffness gradient in the mouse limb bud. Proc Natl Acad Sci U S A. 2020;117: 4781–4791. doi:10.1073/pnas.1912656117

31. Bao Z, Murray JI, Boyle T, Ooi SL, Sandel MJ, Waterston RH. Automated cell lineage tracing in *Caenorhabditis elegans*. Proc Natl Acad Sci U S A. 2006;103: 2707–2712.

32. McDole K, Guignard L, Amat F, Berger A, Malandain G, Royer LA, et al. In Toto Imaging and Reconstruction of Post-Implantation Mouse Development at the Single-Cell Level. Cell. 2018;175: 859-876.e33. doi:10.1016/j.cell.2018.09.031

33. Amat F, Keller PJ. Towards comprehensive cell lineage reconstructions in complex organisms using light-sheet microscopy. Dev Growth Differ. 2013;55: 563–578. doi:10.1111/dgd.12063

34. Kyoda K, Adachi E, Masuda E, Nagai Y, Suzuki Y, Oguro T, et al. WDDD: Worm developmental dynamics database. Nucleic Acids Res. 2013;41: D732-7. doi:10.1093/nar/gks1107

35. Kurotaki Y, Hatta K, Nakao K, Nabeshima Y-I, Fujimori T. Blastocyst Axis Is Specified Independently of Early Cell Lineage But Aligns with the ZP Shape. Science. 2007;316: 719–23. doi:10.1126/science.1138591

36. Podewitz N, Delarue M, Elgeti J. Tissue homeostasis: A tensile state. Epl. 2015;109: 1–6. doi:10.1209/0295-5075/109/58005

37. Cuvelier M, Pešek J, Papantoniou I, Ramon H, Smeets B. Distribution and propagation of mechanical stress in simulated structurally heterogeneous tissue spheroids. Soft Matter. 2021;17: 6603–6615. doi:10.1039/d0sm02033h

38. Arata Y, Takagi H, Sako Y, Sawa H. Power law relationship between cell cycle duration and cell volume in the early embryonic development of Caenorhabditis elegans. Front Physiol. 2015;5: 529. doi:10.3389/fphys.2014.00529

39. Brodland GW, Conte V, Cranston PG, Veldhuis J, Narasimhan S, Hutson MS, et al. Video force microscopy reveals the mechanics of ventral furrow invagination in Drosophila. Proc Natl Acad Sci U S A. 2010;107: 22111–22116. doi:10.1073/pnas.1006591107

40. Ishihara S, Sugimura K. Bayesian inference of force dynamics during morphogenesis. J Theor Biol. 2012;313: 201–211. doi:10.1016/j.jtbi.2012.08.017

41. Drasdo D, Höhme S. A single-cell-based model of tumor growth in vitro: monolayers and spheroids. Phys Biol. 2005;2: 133–147. doi:10.1088/1478-3975/2/3/001

42. Fierro-González JC, White MD, Silva JC, Plachta N. Cadherin-dependent filopodia control preimplantation embryo compaction. Nat Cell Biol. 2013;15: 1424–33. doi:10.1038/ncb2875

43. Yamanaka Y, Ralston A, Stephenson RO, Rossant J. Cell and molecular regulation of the mouse blastocyst. Dev Dyn. 2006;235: 2301–2314. doi:10.1002/dvdy.20844

44. Edgar LG. Blastomere Culture and Analysis. Methods Cell Biol. 1995;48: 303–321. doi:10.1016/S0091-679X(08)61393-X

45. Schierenberg E, Junkersdorf B. The role of eggshell and underlying vitelline membrane for normal pattern formation in the early C. elegans embryo. Roux's Arch Dev Biol. 1992;202: 10–16. doi:10.1007/BF00364592

46. Kim J, Lee J, Choi YJ, Kwon O, Lee TB, Jun JH. Evaluation of morphokinetic characteristics of zona pellucida free mouse pre-implantation embryos using time-lapse monitoring system. Int J Dev Biol. 2020;64: 415–422. doi:10.1387/ijdb.190188jj

47. Maître J-L, Niwayama R, Turlier H, Nédélec F, Hiiragi T. Pulsatile cell-autonomous contractility drives compaction in the mouse embryo. Nat Cell Biol. 2015;17: 849–855. doi:10.1038/ncb3185

48. Takeichi M. The cadherins : cell-cell adhesion molecules controlling animal morphogenesis. 1988;655.

49. Mombach JCM, Robert D, Graner F, Gillet G, Thomas GL, Idiart M, et al.

Rounding of aggregates of biological cells : Experiments and simulations. Physica A. 2005;352: 525–534. doi:10.1016/j.physa.2005.02.008

50. Manning ML, Foty RA, Steinberg MS, Schoetz E-M. Coaction of intercellular adhesion and cortical tension specifies tissue surface tension. Proc Natl Acad Sci. 2010;107: 12517–12522. doi:10.1073/pnas.1003743107

51. Mgharbel A, Delanoë-ayari H, Rieu J. Measuring accurately liquid and tissue surface tension with a compression plate tensiometer. HFSP J. 2009;3: 213–221. doi:10.2976/1.3116822

52. Petridou NI, Corominas-Murtra B, Heisenberg CP, Hannezo E. Rigidity percolation uncovers a structural basis for embryonic tissue phase transitions. Cell. 2021;184: 1914-1928.e19. doi:10.1016/j.cell.2021.02.017

53. Honda H, Motosugi N, Nagai T, Tanemura M, Hiiragi T. Computer simulation of emerging asymmetry in the mouse blastocyst. Development. 2008;135: 1407–1414. doi:10.1242/dev.014555

54. Belmonte JM, Clendenon SG, Oliveira GM, Swat MH, Greene E V., Jeyaraman S, et al. Virtual-tissue computer simulations define the roles of cell adhesion and proliferation in the onset of kidney cystic disease. Mol Biol Cell. 2016;27: 3673–3685. doi:10.1091/mbc.e16-01-0059

55. Nonomura M. Study on multicellular systems using a phase field model. PLoS One. 2012;7: 1–9. doi:10.1371/journal.pone.0033501

56. Camley BA, Zhang Y, Zhao Y, Li B, Ben-Jacob E, Levine H, et al. Polarity mechanisms such as contact inhibition of locomotion regulate persistent rotational motion of mammalian cells on micropatterns. Proc Natl Acad Sci U S A. 2014;111: 14770–14775. doi:10.1073/pnas.1414498111

57. Dokmegang J, Yap MH, Han L, Matteo C, Doursat R. Computational modelling unveils how epiblast remodelling and positioning rely on trophectoderm morphogenesis during mouse implantation. PLoS One. 2021;16: e0254763. doi:10.1371/journal.pone.0254763

58. Kajita A, Yamamura M, Kohara Y. Computer simulation of the cellular arrangement using physical model in early cleavage of the nematode Caenorhabditis elegans. Bioinformatics. 2003;19: 704–716. doi:10.1093/bioinformatics/btg069

59. Tambe DT, Hardin CC, Angelini TE, Rajendran K, Park CY, Serra-Picamal X, et al. Collective cell guidance by cooperative intercellular forces. Nat Mater. 2011;10: 469–75. doi:10.1038/nmat3025

60. Vitorino P, Hammer M, Kim J, Meyer T. A Steering Model of Endothelial Sheet

Migration Recapitulates Monolayer Integrity and Directed Collective Migration. Mol Cell Biol. 2011;31: 342–350. doi:10.1128/MCB.00800-10

61. Liu S, Lemaire P, Munro E, Mani M. A mathematical theory for the mechanics of three-dimensional cellular aggregates reveals the mechanical atlas for Ascidian embryogenesis. bioRxiv. 2022. Available: https://doi.org/10.1101/2022.11.05.515310

62. Bi D, Yang X, Marchetti MC, Manning ML. Motility-driven glass and jamming transitions in biological tissues. Phys Rev X. 2016;6: 021011. doi:10.1103/PhysRevX.6.021011

63. Durney CH, Feng JJ. A three-dimensional vertex model for Drosophila salivary gland invagination. Phys Biol. 2021;18: 046005. doi:10.1088/1478-3975/abfa69

64. Germann P, Marin-Riera M, Sharpe J. ya||a: GPU-Powered Spheroid Models for Mesenchyme and Epithelium. Cell Syst. 2019;8: 261–266. doi:10.1016/j.cels.2019.02.007

65. Trepat X, Sahai E. Mesoscale physical principles of collective cell organization. Nat Phys. 2018;14: 671–682. doi:10.1038/s41567-018-0194-9

66. Smutny M, Ákos Z, Grigolon S, Shamipour S, Ruprecht V, Čapek D, et al. Friction forces position the neural anlage. Nat Cell Biol. 2017;19: 306–317.

doi:10.1038/ncb3492

67. Koyama H, Suzuki M, Yasue N, Sasaki H, Ueno N. Differential Cellular Stiffness Contributes to Tissue Elongation on an Expanding Surface. Front Cell Develpmental Biol. 2022;10: 864135. doi:10.3389/fcell.2022.864135

68. Aoki K, Kondo Y, Honda N, Hiratsuka T, Itoh RE, Matsuda M. Propagating Wave of ERK Activation Orients Collective Cell Migration. Dev Cell. 2017;43: 305–317. doi:10.1016/j.devcel.2017.10.016

69. Ryan PL, Foty RA, Kohn J, Steinberg MS. Tissue spreading on implantable substrates is a competitive outcome of cell–cell vs . cell–substratum adhesivity. Proc Natl Acad Sci U S A. 2001;98: 4323–4327.

Figures

Figure 1: Overview of strategy for inferring the effective potential of cell–cell interactions

A. Relationship between microscopic forces and attractive/repulsive forces in isolated two cell systems. i) Microscopic forces are exemplified. ii) The microscopic forces are approximated as attractive/repulsive forces where cells are described as particles with the mean size. iii) Both the repulsive and attractive forces are provided as cell–cell distance-dependent functions, and the summation (black broken line) is the distance–force curve of the two particles. The relationship between the curve and the mean diameters of the cells is shown. iv) A distance–potential curve is shown where the mean diameters of cells correspond to the distance at the potential minimum.

B. Strategy for inferring effective forces of cell–cell interactions. i) Particle model. A blue sphere corresponds to a cell. Attractive or repulsive force between the particles (blue spheres #1–4), was considered; vectors of cell–cell interaction forces (F_i) are illustrated by black arrows in the case of particle #3. The net force ($F_{C|p}$) of particle #3 is shown by a red vector. The summation of F_i results in $F_{C|p}$ which determines the velocity ($V_{C|p}$) of pth particle. ii) Nuclear tracking data were obtained and used as a reference data during the inference. iii) Effective forces of cell–cell interactions were inferred by fitting. Red line, attractive; blue line, repulsive. iv) From the inferred effective forces, we examined

whether distance–force/potential curves are detected.

Related figure: Figure S1 (inference method).

Figure 2: Validation of inference method using simulation data

Simulations were performed on the basis of a distance–force (DF) curve obtained from the Lenard-Jones potential (LJ). The DF curve is shown in A-i. The simulation conditions contain “Assembling process” (A), “Steady state” (B), and “Cell proliferation” (C). For A-C, snapshots of the simulations are shown where the particles are of the mean size of cells (i). In A-ii, the procedure of data analyses is exemplified, where a colored heat map representing the frequencies of the data points (Frequency index (FI)). Averaged values of the forces are shown in yellow (binned average). In A-iii, B-ii, and C-ii, the resultant effective DF curves are shown with the DF curves from the LJ potential. Normalized L2 norms = $\{F_{\mathrm{inferred}}(D) - F_{\mathrm{LJ}}(D)\}^2 / (F_{\mathrm{LJ_max}})^2$ were calculated along D, and then the mean values along D were calculated; $F_{\mathrm{LJ_max}}$ is the maximum attractive force in the LJ potential, and the range of D was set that the absolute values of attractive forces at D are $\geq (0.1 \times |F_{\mathrm{LJ_max}}|)$. The normalize L2 norms are: in A-iii, 0.035 (0%), 0.034 (10%), 0.033 (100%), and 0.024 (1000%); in B-ii, 0.032 (1min), 0.046 (3min), and 0.15 (5min); in C-ii, 0.068

848 (1min), 0.035 (3min), and 0.095 (10min).

849 Related figures: Figure S2 and S3 (in the case of other given potential and random walk).

850

851

852 Figure 3: Influence of external constraints to effective forces of cell–cell interaction

853 Spherocylindrical constraints corresponding to eggshells are assumed in the particle

854 model used in Fig. 2. i) An example of simulations with labeling three cells (red, yellow,

855 and green). For the condition of the spherocylindrical length = 16μm ("compressive"),

856 the array of particles is marked by broken lines. ii) Inferred DF curves. The normalize L2

857 norms defined in Fig. 2 are: 0.062 (40μm), 0.066 (30μm), 0.077 (25μm), 0.16 (20μm),

858 and 0.29 (16μm).

859 Related Figures: Figure S4 (inference under spherical constraints) and S5 (inference in

860 spherocylindrical constraints).

861

862

863 Figure 4: Inference of effective force of cell–cell interaction in *C.elegans* embryos

864 A. Snapshot of the nuclear positions in the *C.elegans* embryo with cell lineages at time

865 frame = 76.

866 B. Mean diameters of cells at each time frame estimated from cell numbers. Given that
867 the volume of the embryos is constant (= *Vol*) during embryogenesis, the mean diameters
868 were estimated from the cell numbers (N_c) at each time frame as follows: mean diameter
869 = $\{Vol / (4/3\ \pi\ N_c)\}^{1/3}$. The diameters relative to that at time frame = 16 are shown with
870 cell numbers. The sizes of the circles reflect the diameters, whose colors roughly
871 correspond to the colors in the graph in F.
872 C. Snapshots with inferred effective forces with the force values described by colored
873 lines at t = 16, 76, and 195. Forces are depicted in arbitrary units (A.U.); 1 A.U. of the
874 force can move a particle at 1μm/min. The nuclear tracking data were obtained from a
875 previous report [31].
876 D. Uniqueness of solution of effective force inference was examined. The minimizations
877 of the cost function G were performed from different initial force values as described in
878 the x- and y- axes, and the inferred values of each cell-cell interaction were plotted by
879 crosses.
880 E. The inferred effective forces of cell–cell interactions were plotted against the distance
881 of cell–cell interactions with binned averages at t = 76-115.
882 F. Inferred DF and DP curves at various time frames.
883 G. DP curves normalized by the distances at the potential minima at various time frames.

Related figure: Figure S6 (uniqueness of solution was examined), S7 (the inferred DP curves were fitted by previously used frameworks such as the Morse potential), and S8 (inferred potentials under the relative velocity-based model).

Related movies: Movie S1A (tracking data) and S1B (force map).

Figure 5: Inference of the effective force of cell–cell interaction in mouse pre-implantation embryos

A. Eight-cell and compaction stages of mouse embryo are illustrated, and their confocal microscopic images are shown: bright field, maximum intensity projection (MIP) and cross-section of fluorescence of H2B-EGFP. Snapshots of nuclear tracking are also shown; blue spheres indicate the detected nuclei. Scale bars = 15μm.

B. Inferred DF and DP curves.

Related figures: Figure S9 (data from other embryos) and S10 (DF and DP curves in the outer and inner cells in the compaction stage).

Related movies: Movie S2A-B (tracking data) and Movie S2C-D (force maps)

Figure 6: Outcomes of simulations based on inferred distance–force curves

A. Simulations results under the DF curves derived from *C. elegans* and mouse embryos are exemplified.

B and C. DF curves sampled before reaching the minima of *G*, and simulation outcomes. DF curves, left panels; the values of *G* and the maximum attractive forces in the DF curves, right panels; simulation outcomes for each DF curve with the initial configuration ("start"), bottom panels. The values of *G* are relative to that in the case of all forces = 0. The colors in each three panels in B and C correspond each other. In the right panels, the numbers of the data points are 14 and 12 in B and C, respectively, and the representative ones (colored circles) are selected for presenting the DF curves and the simulation outcomes.

Figure 7: Inference of effective potentials of cell–cell interaction in compaction-inhibited mouse embryos

A. Microscopic images of embryos under chemicals. CytoD, cytochalasin D; Bleb, blebbistatin.

920 B. Inferred DP curves in the drug-treated embryos. N=6~10 for each condition.

921 C. Quantitative differences in the DP curves. Distances at the potential minima in the DP

922 curves, left panel; Distances providing 10% energy of the potential minima as the relative

923 value to the distances at the potential minima, right panel. Mann–Whitney–Wilcoxon tests

924 were performed and the resultant *p*-values for "No Drugs" vs. "EDTA", vs. "CytoD", and

925 vs. "Bleb" are 0.011, 0.23, and 0.00040, respectively, in the left panel. In the right panel,

926 distances providing other % energies instead of 10% are shown in Fig. S14B.

927 D. Confocal microscopic images of cell shapes. Cell shapes were visualized by staining

928 F-actin or E-cadherin.

929 E. The embryonic and cellular shapes illustrated based on D.

930 Related figures: Figure S11 (experimental design), S12 (enlarged view of DP curves), S13

931 (histological images of other embryos), and S14 (details of quantification of DP curves).

932

933

934 Figure 8: Simulations under inferred distance–potential curves in drug-treated embryos,

935 and identification of parameters explaining morphological transition

936 A. Simulation results for the drug-treated embryos. All simulation data are provided in

937 Figure S15A, and the representative results which nearly showed the mean values of the

938 sphericities for each condition are chosen here.

939 B. Sphericities in the simulations of the drug-treated embryos (left panel), and the

940 sphericities plotted against the distances at the potential minima calculated in Figure 7C.

941 Mann–Whitney–Wilcoxon tests were performed: *p*-values for "No Drugs" vs. "EDTA",

942 vs. "CytoD", and vs. "Bleb" are 0.011, 1.0, and 0.00080, respectively.

943 C. Aspect ratios in simulations of the drug-treated embryos (left panel), and the aspect

944 ratios plotted against the relative distances providing 10% energy of the potential minima

945 calculated in Figure 7C. Mann–Whitney–Wilcoxon tests were performed: *p*-values for

946 "No Drugs" vs. "EDTA", vs. "CytoD", and vs. "Bleb" are 0.21, 0.97, and 0.33,

947 respectively.

948 Related figures: Figure S15 (all simulation outcomes).

949

950

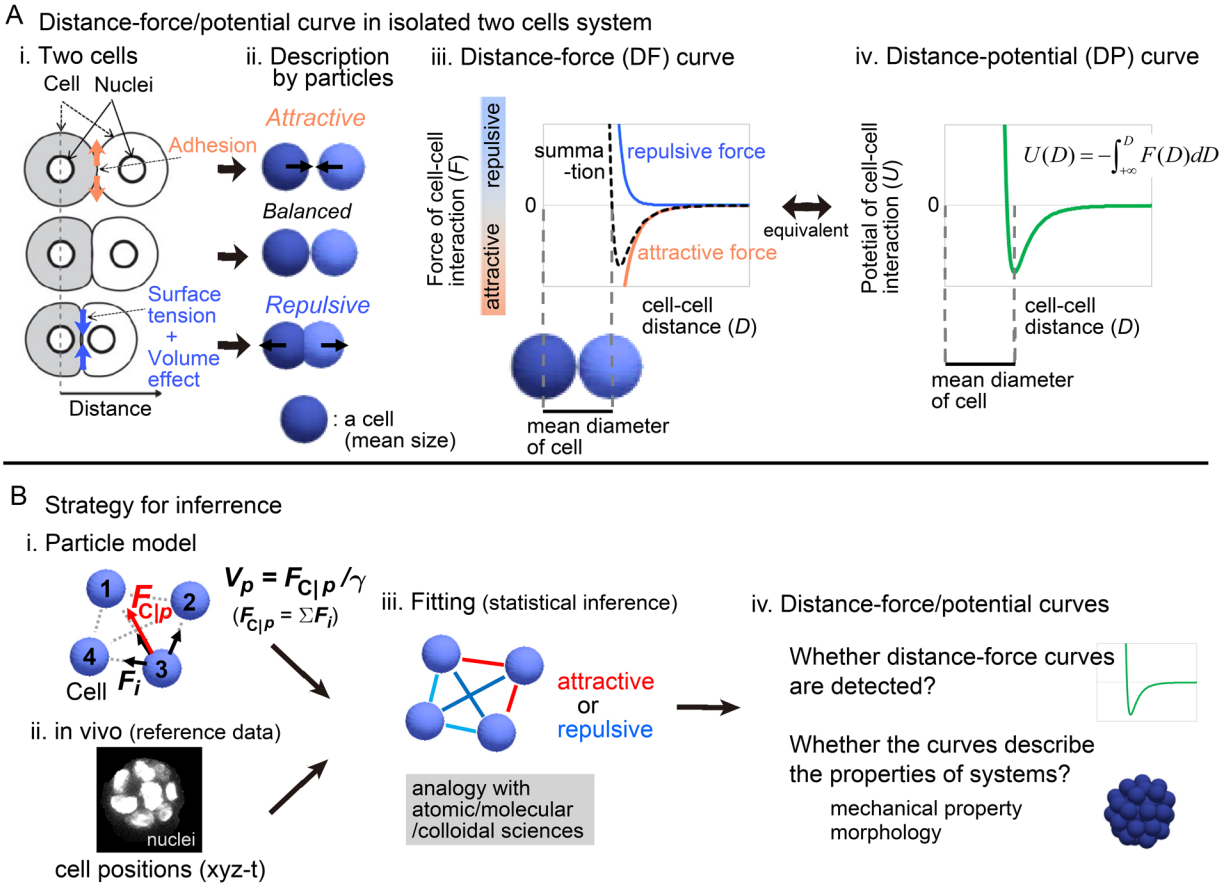

Fig.1 Koyama et al.

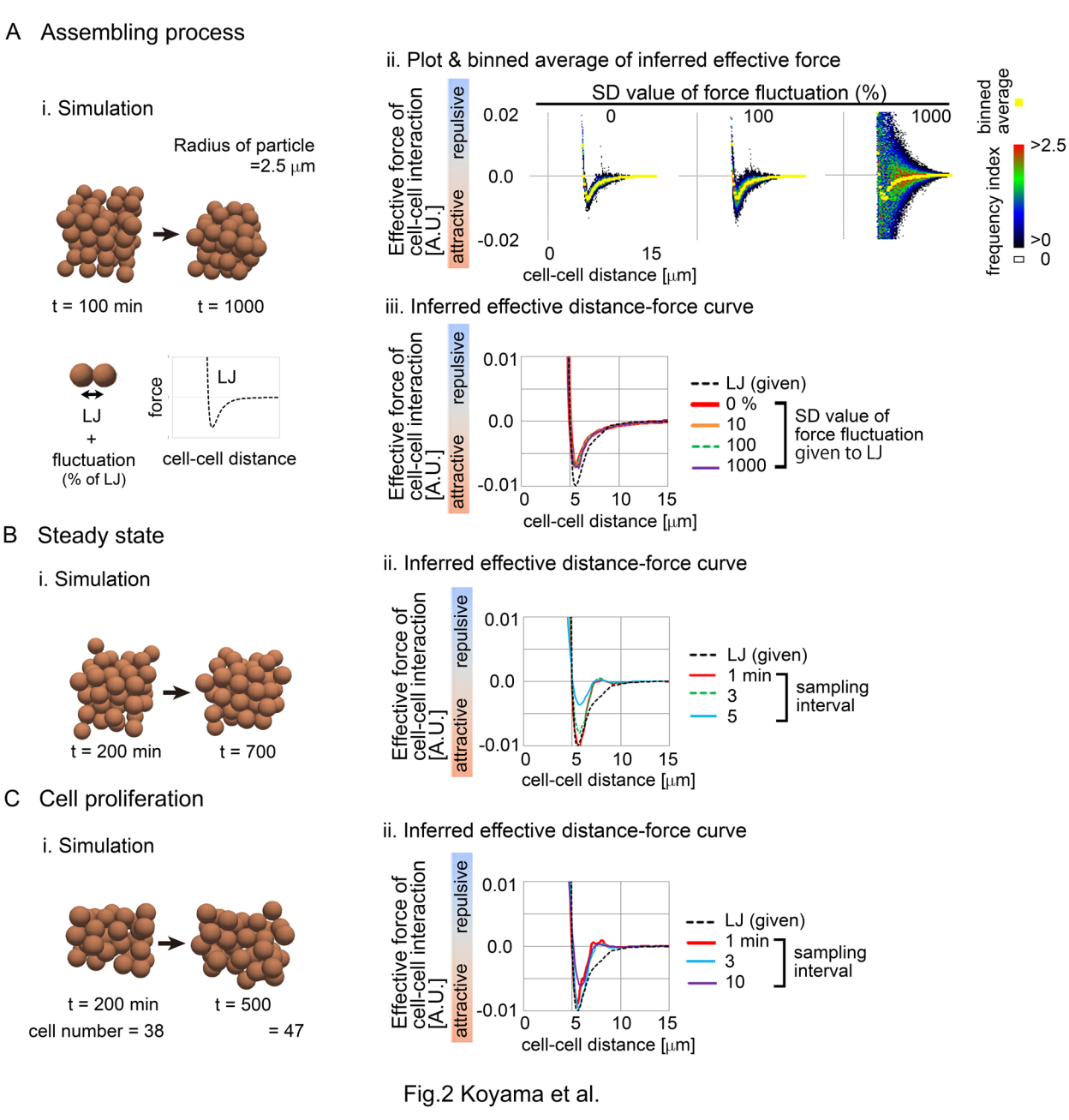

Fig.2 Koyama et al.

Egg shell-like spatial constraints: spherocylinder

i. Simulation

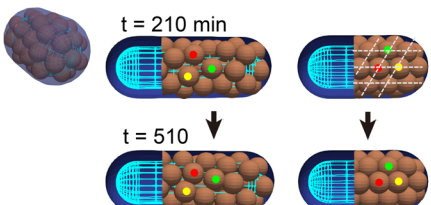

length of spherocylinder = 25 μm

16 μm (compressive)

radius of spherocylinder = fixed (7.5 μm)

ii. Inferred effective distance-force curve

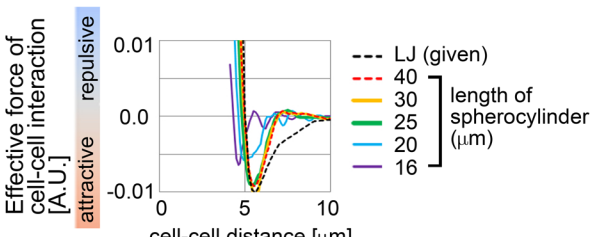

Fig.3 Koyama et al.

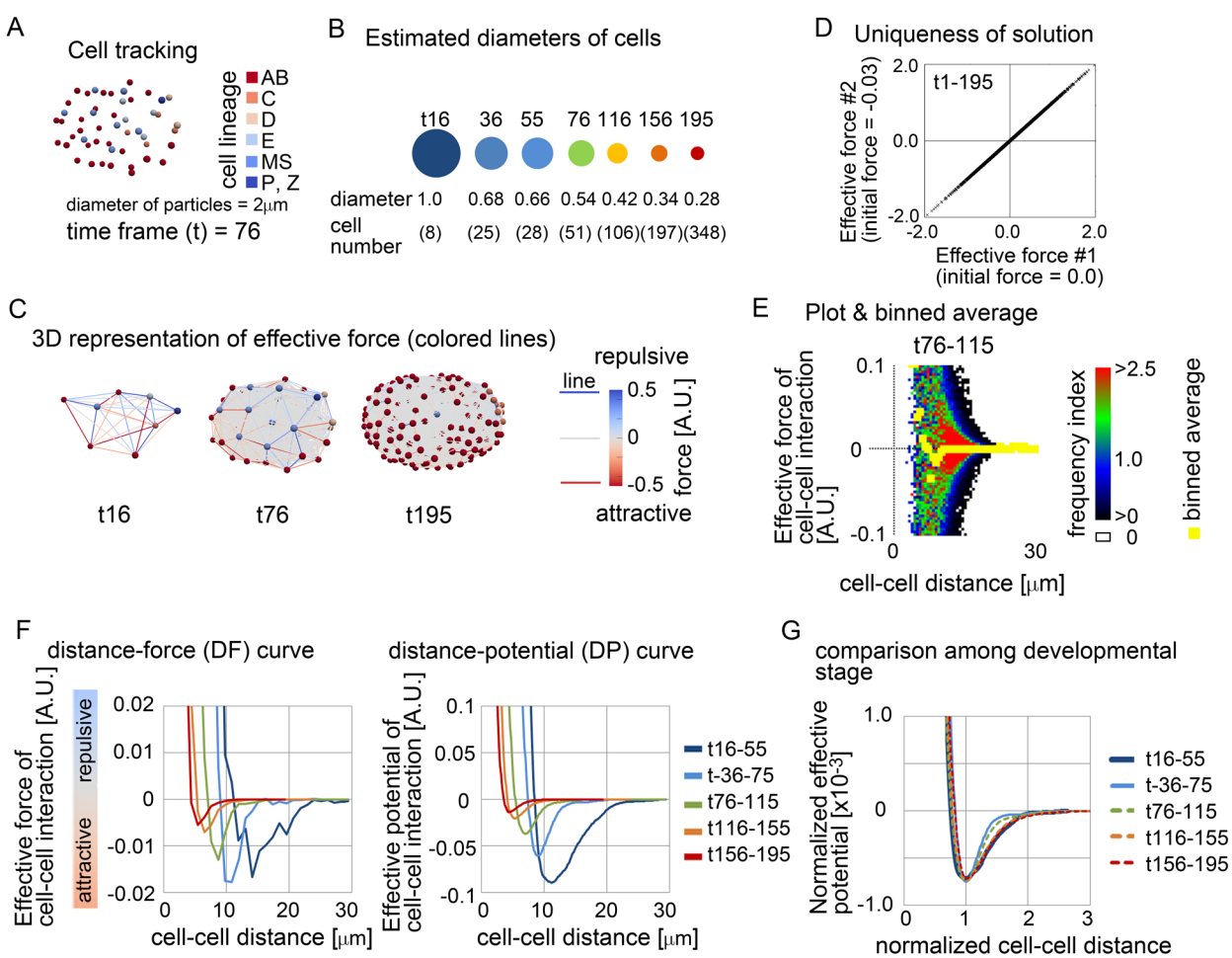

Fig.4 Koyama et al.

A

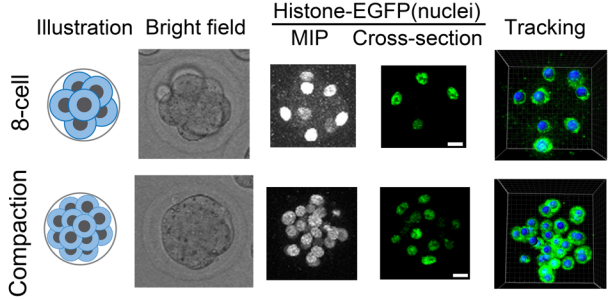

B

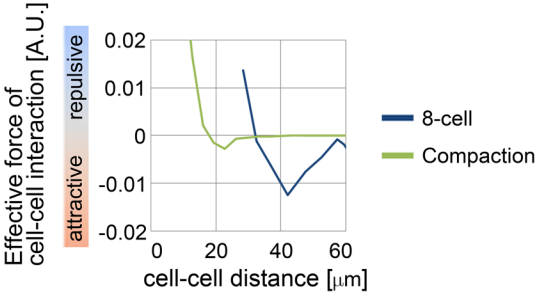

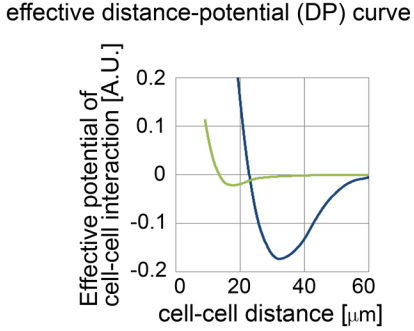

Fig. 5 Koyama et al.

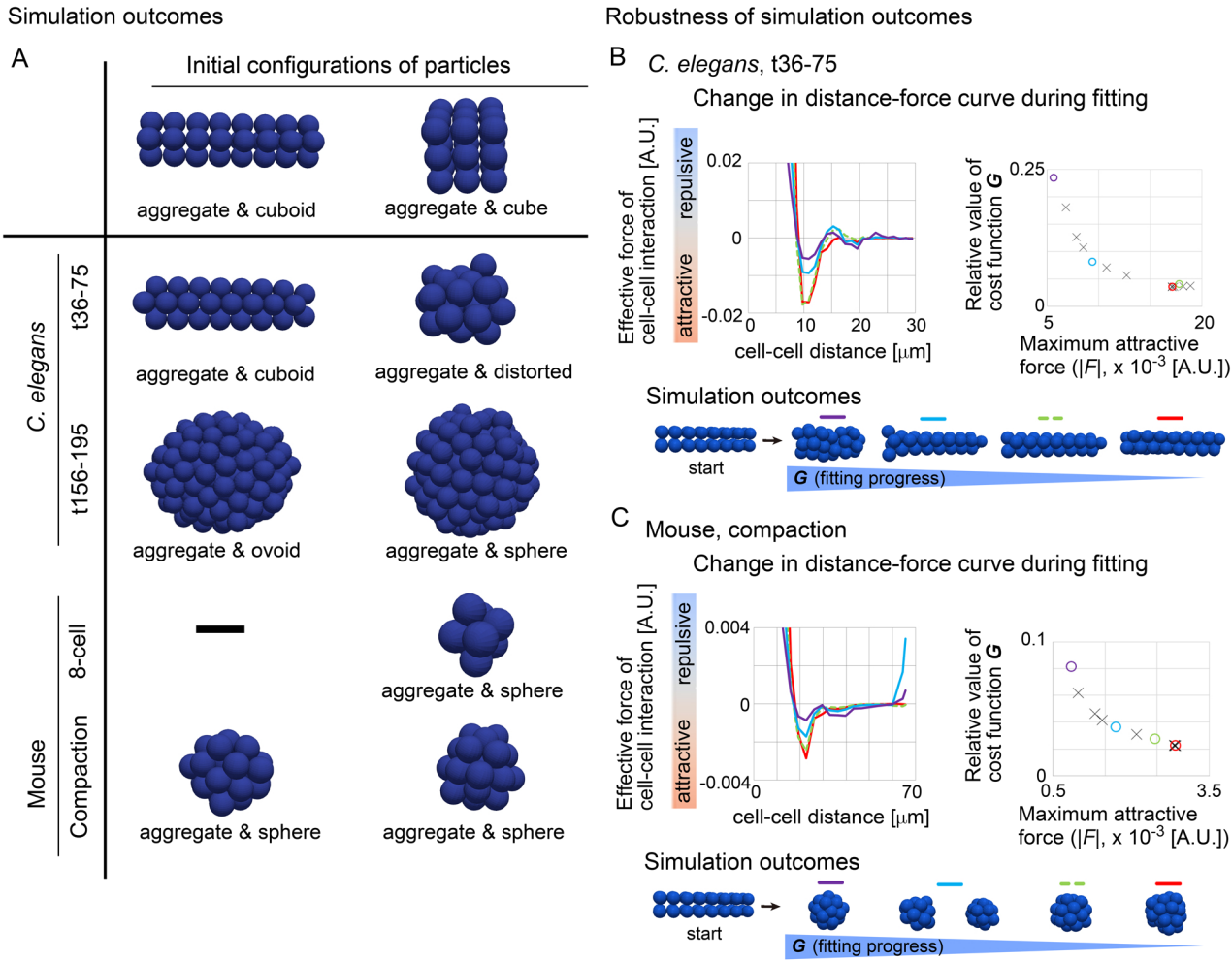

Fig.6 Koyama et al.

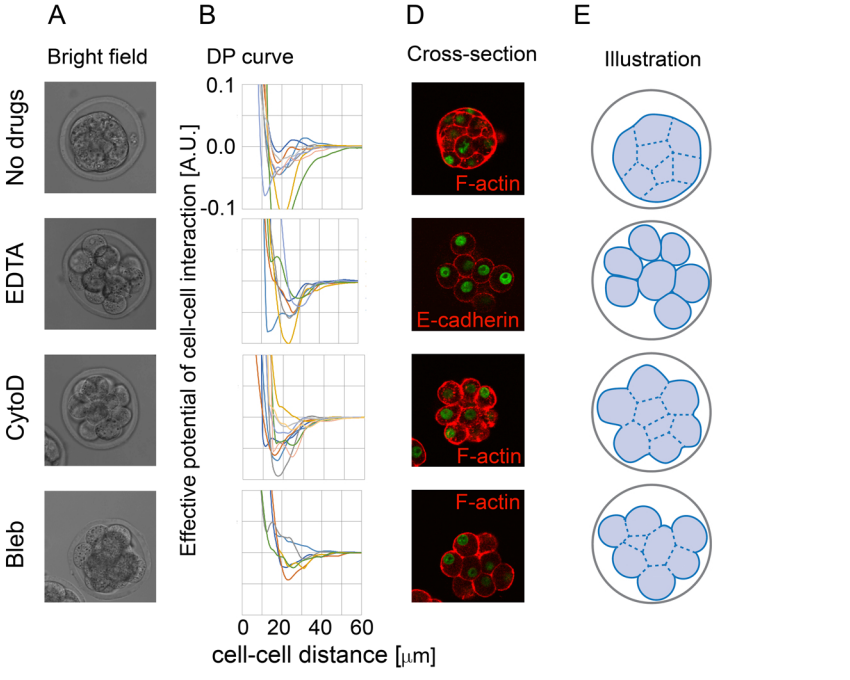

C Quantitative differences in DP curves

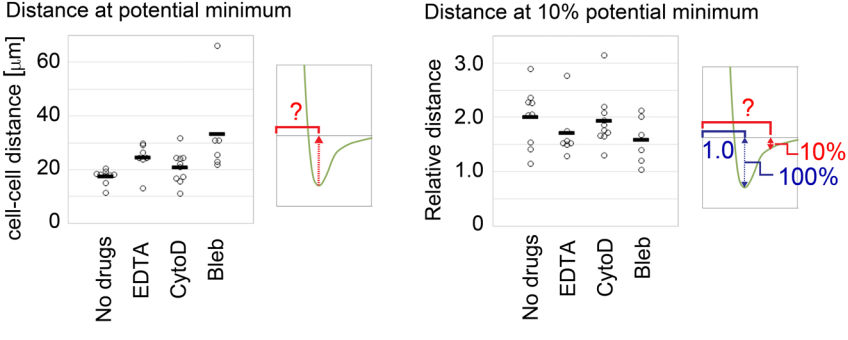

Fig.7 Koyama et al.

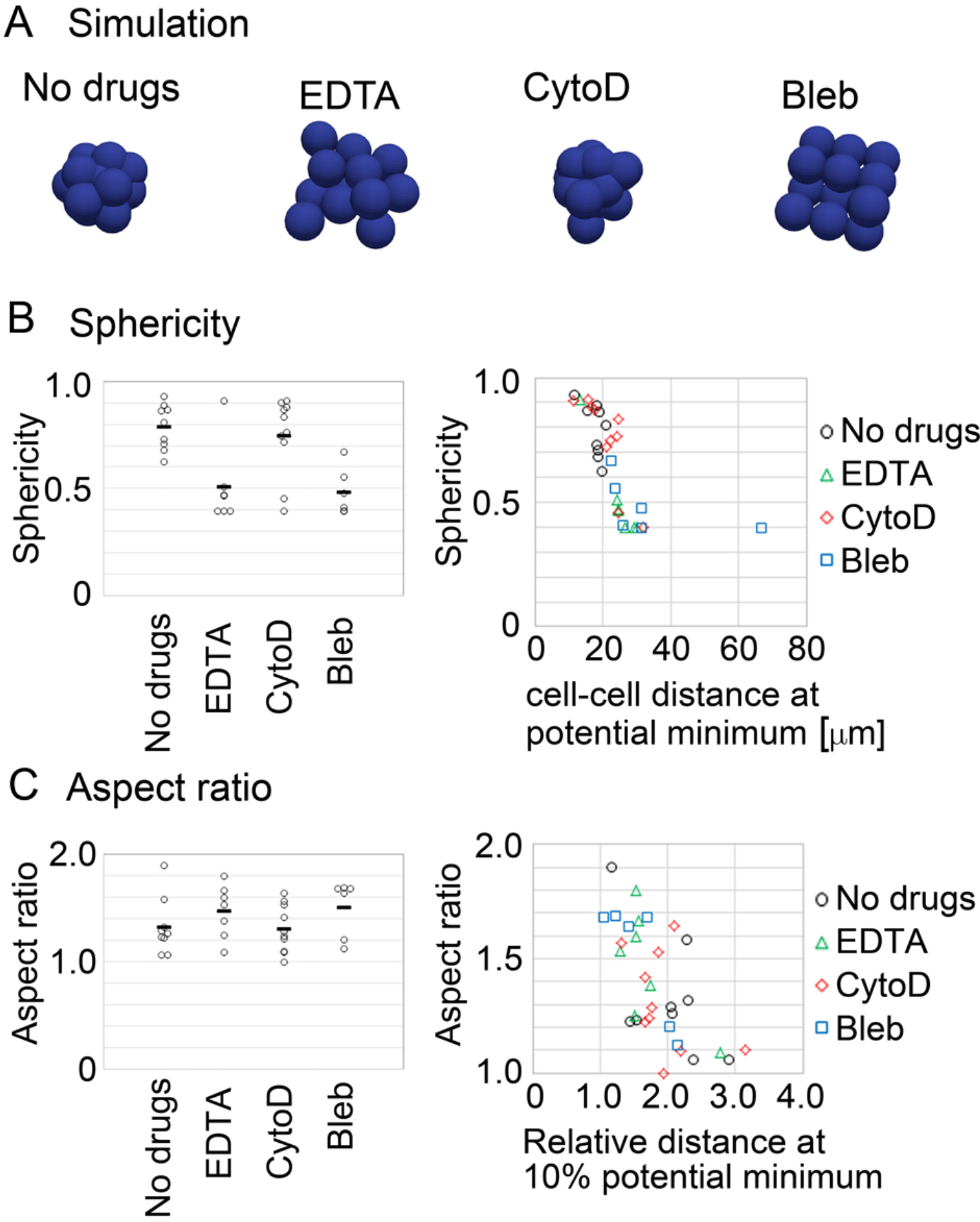

Fig.8 Koyama et al.